

UC Berkeley

UC Berkeley Previously Published Works

Title

Jahn-Teller Assisted Na Diffusion for High Performance Na Ion Batteries

Permalink

<https://escholarship.org/uc/item/9j91n22f>

Journal

Chemistry of Materials, 28(18)

ISSN

0897-4756

Authors

Li, Xin
Wang, Yan
Wu, Di
[et al.](#)

Publication Date

2016-09-27

DOI

10.1021/acs.chemmater.6b02440

Peer reviewed

Jahn–Teller Assisted Na Diffusion for High Performance Na Ion Batteries

Xin Li,[†] Yan Wang,[‡] Di Wu,[§] Lei Liu,[‡] Shou-Hang Bo,^{‡,||} and Gerbrand Ceder^{*,||,⊥}

[†]John A. Paulson School of Engineering and Applied Sciences, Harvard University, Cambridge, Massachusetts 02138, United States

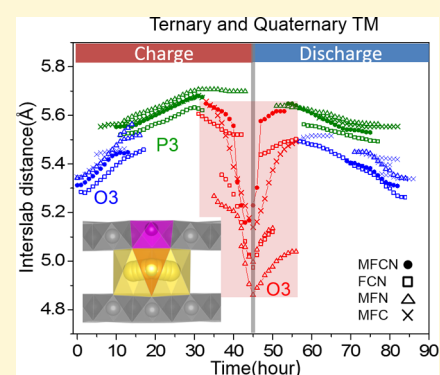
[‡]Department of Materials Science and Engineering, Massachusetts Institute of Technology, Cambridge, Massachusetts 02139, United States

[§]Department of Mechanical Engineering, Massachusetts Institute of Technology, Cambridge, Massachusetts 02139, United States

^{||}Materials Science Division, Lawrence Berkeley National Laboratory, Berkeley, California 94720, United States

[⊥]Department of Materials Science and Engineering, University of California, Berkeley, California 94720, United States

ABSTRACT: Na energy storage technology is strategically attractive for large scale applications such as grid energy storage. We show in this paper that there is a clear relation between the Jahn–Teller activity of a transition metal ion at the end of charge and the mobility of Na in a cathode material. This is particularly important as mobility at the end of charge limits the capacity of current materials. Hence, by using this classical piece of physics in the battery world, it is possible to create higher capacity Na-cathode materials. Even more exciting is that the ideal element to impart this effect on cathodes is Fe, which is the least expensive of the transition metal oxides and can therefore enable low cost cathode materials.



1. INTRODUCTION

Sodium (Na) ion batteries have attracted increasing interest recently as an alternative option to lithium (Li) ion batteries. Na resources have a more homogeneous global geographical distribution and are generally less expensive than lithium.^{1–4} This makes Na energy storage technology strategically attractive, especially for large scale applications such as grid energy storage. Layered NaTMO₂ (TM: transition metal) is the most competitive cathode compound in terms of capacity, energy density, and rate capability, with some cathodes already showing energy density well above 500 Wh/kg.^{5–7} These layered Na-compounds can be synthesized from a broad choice of 3d transition metal elements from Ti to Cu, as well as their combinations,^{5–27} while the lithium analogs are limited to combinations of Co, Ni, and Mn.²⁸ This broader choice of transition metal elements can reduce the large contribution of materials to the cost of today's lithium-ion technology.^{2,4,24} We show in this paper that the ability for Na cathodes to use Fe as an active component is another major advantage over Li-technology. We demonstrate that a unique interplay between the Jahn–Teller physics of Fe⁴⁺O₆ octahedron and Na diffusion maintains Na mobility up to a very high charge level, thereby endowing Fe-containing cathodes not only with low cost but also with very high capacity. As such, we believe that this is the first and remarkably practical application of this classical physics of TM ions into layered energy storage compounds in the energy field.

The limiting factors for the performance of sodium layered electrodes are the inaccessible capacity in the high voltage range and the significant deterioration of cyclability at high cutoff voltage. The former situation limits the capacity directly,^{15,17} while the latter leads to a quick decay of the capacity from its high initial value.⁶ This problem arises from the layer spacing collapse which occurs when most of the alkaline ions in either Na or Li layered cathodes are extracted, leading to reduced alkali mobility.^{29,30} This fundamental limit to the practical capacity of layered oxides has been difficult to overcome and inhibits cathodes to approach their theoretical energy density. Our work is inspired by the recent discovery of Na-cathode materials with high capacity, all of which contain Fe. For example, compounds such as Na(Mn_{0.25}Fe_{0.25}Co_{0.25}Ni_{0.25})O₂ (MFCN) delivers much higher capacity and better cyclability than others like NaNiO₂¹⁵ or Na(Fe_{0.5}Co_{0.5})O₂ (FC) at high cutoff voltage.⁶

In this paper, we use layered NaTMO₂ compounds as model systems to demonstrate that the unique capability to stabilize the Fe³⁺O₆/Fe⁴⁺O₆ redox-couple in layered sodium structure is the critical factor to reach optimal battery performance. We identify a new mechanism of Jahn–Teller distortion assisted sodium diffusion which greatly improves the Na diffusivity through a soft-mode buckling of the Jahn–Teller high-spin

Received: June 16, 2016

Revised: August 26, 2016

Fe^{4+}O_6 octahedron. The new mechanism could potentially be applied to any type of sodium intercalation compound whenever the Jahn–Teller active transition metal is face-sharing with the activated site for sodium diffusion, including channeled³¹ and zigzag layered structures.³²

A Jahn–Teller (JT) distortion lowers the energy of a system by certain bond length distortions to break the local crystal symmetry and lift the degeneracy of the electronic system.^{33,34} Among the 3d transition metal ions, Mn^{3+} , Fe^{4+} , and Ni^{3+} in octahedral coordination show the strongest JT effect.^{33,35} The uniqueness of Fe originates from the fact that it is the only 3d transition metal element that becomes JT active at the end of charge in Na_xTMO_2 when the TM is oxidized to 4+, while Mn^{4+} and Ni^{4+} lose their JT activity in the 4+ state, as illustrated in Figure 1. We will demonstrate through detailed

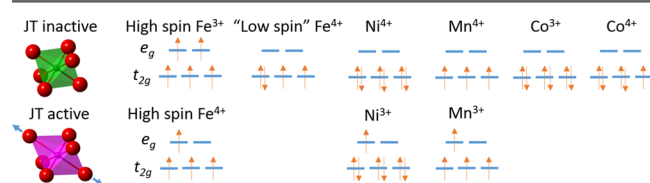


Figure 1. Electronic structures of Jahn–Teller inactive (top row) and active (bottom row) transition metal oxide octahedrons.

simulation and experimental characterization that it is the JT activity of Fe^{4+}O_6 that lowers the Na diffusion barrier at the later stage of charge and enables the extraction of more sodium ions.

2. METHODS

2.1. Synthesis and Electrochemical Testing. All the sodium layered compounds were synthesized using solid state reaction by mixing either Na_2O_2 or Na_2CO_3 with the transition metal oxides precursors, following the methods in the previous literature.^{6,7,9,13–15,17,19,21–23} The new compound O3-MFC was synthesized by sintering at 900 °C for 12 h the pellet that was cold pressed from the ball milled mixture of a stoichiometric amount of Na_2CO_3 , Mn_2O_3 , Fe_2O_3 , and Co_3O_4 powders. The cathode film was made by mixing as-synthesized powder, Super P carbon black (Timcal), and dry PTFE (DuPont) with the weight ratio of 80:15:5. A Swagelok battery was assembled using glass fiber (Whatman GF/F) as separator, Na metal (99.95% Sigma-Aldrich) as anode, and 1 M NaPF_6 (98%, Sigma-Aldrich) in EC/DEC (anhydrous, 1:1 volume ratio) as electrolyte with the moisture level less than 3 ppm. The galvanostatic cycling was tested on Solartron 1470E at C/10 rate in the voltage range of 2.0–4.5 V on the cathode film with the loading density around 2 mg/cm². MFC was cycled between 1.5 and 4.5 V due to its relatively low average voltage.

2.2. In Situ XRD (X-ray Diffraction). The *in situ* lab XRD was taken on Bruker D8 X-ray diffractometer equipped with a Mo source from a homemade *in situ* electrochemical cell with Be window. The *in situ* cell was charged galvanostatically at C/50 rate between 2.0 and 4.5 V on Solartron 1287 with each XRD pattern scanned from 6.5° to 30.5° 2θ angle range (equivalent to 14.1° to 69.7° on Cu source) for 1 h, corresponding to 2% Na composition resolution per pattern. The phases in the *in situ* XRD spectra were identified by XRD refinement. MFC was cycled between 1.0 and 4.5 V due to its relatively low average voltage.

2.3. TEM (Transmission Electron Microscopy). A Swagelok battery cell was disassembled inside the glovebox, where the cathode film was sonicated in DMC solution (dimethyl carbonate) and dropped onto the TEM copper grid. The TEM sample was sealed in an airtight bottle in the glovebox before loading into the TEM column. The HRETM and electron diffraction measurements were performed on JEOL 2010F.

2.4. Synchrotron XRD Refinement. To extract the lattice symmetry and dimensions of the cycled NaFeO_2 , the corresponding synchrotron X-ray diffraction pattern was collected from NaFeO_2 cathode film electrochemically charged to 4.5 V and then discharged to 2 V. The sodium content after 1 cycle is around $\text{Na}_{0.5}\text{FeO}_2$ estimated from the difference between charge and discharge capacities. The synchrotron XRD pattern was analyzed through Pawley fits using the Bruker TOPAS software package. We chose five different lattices to fit the diffraction pattern, based on the observation of electron diffraction measurements and the most commonly observed structures reported in prior literature. Specifically, three of these lattices are the spinel ($Fd\bar{3}m$), hexagonal-distorted spinel ($R\bar{3}m$), and tetragonal-distorted spinel ($I4_1/amd$), with the other two being the O3 ($R\bar{3}m$) and O'3 ($C2/m$) lattices. The lattice parameters and figure-of-merit for the fits (i.e., R_{wp}) are listed in Table 2. Although the best fit was achieved with

Table 1. Initial Discharge Capacity and Energy Density of Different Layered O3- NaTMO_2 Compounds Cycled between 2 and 4.5 V at C/10 Rate^a

compound		1 st discharge capacity (mAh/g)	energy density (Wh/kg)
$\text{Na}(\text{Mn}_{1/4}\text{Fe}_{1/4}\text{Co}_{1/4}\text{Ni}_{1/4})\text{O}_2$	[MFCN]	185	596
$\text{Na}(\text{Fe}_{1/3}\text{Co}_{1/3}\text{Ni}_{1/3})\text{O}_2$	[FCN]	180	545
$\text{Na}(\text{Mn}_{1/3}\text{Fe}_{1/3}\text{Co}_{1/3})\text{O}_2$	[MFC]	180	533
$\text{Na}(\text{Mn}_{1/3}\text{Fe}_{1/3}\text{Ni}_{1/3})\text{O}_2$	[MFN]	185	592
$\text{Na}(\text{Mn}_{1/2}\text{Fe}_{1/2})\text{O}_2$	[MF]	153	424
$\text{Na}(\text{Co}_{1/2}\text{Ni}_{1/2})\text{O}_2$	[NC]	135	414
$\text{Na}(\text{Fe}_{1/2}\text{Ni}_{1/2})\text{O}_2$	[FN]	140	430
$\text{Na}(\text{Fe}_{1/2}\text{Co}_{1/2})\text{O}_2$	[FC]	159	498
NaNiO_2	[Ni]	147	454
NaCoO_2	[Co]	127	398
NaFeO_2	[Fe]	0	0

^aMFC is cycled between 1.5 and 4.5 V due to its low average voltage. Energy density is calculated by multiplying initial discharge capacity and average voltage for each compound. All listed values are from this work.

the use of a monoclinic lattice (O'3, $C2/m$), the fitting error based on the tetragonal distorted spinel is only marginally higher (8.13 vs 8.08). Considering the much higher symmetry of the tetragonal lattice and the much fewer parameters needed in the refinement (2 vs 4) compared to the monoclinic $C2/m$ lattice, we conclude this pattern can be most appropriately indexed with a tetragonal-distorted spinel lattice. This finding is consistent with the electron diffraction measurements where a distorted spinel-like structure was observed.

2.5. Computational. First-principles calculations were performed using density functional theory implemented in the plane-wave-basis-set Vienna ab initio simulation package (VASP).³⁶ Projector augmented wave potentials with kinetic energy cutoff of 520 eV were employed in all simulations. All calculations were spin-polarized starting from a high-spin ferromagnetic configuration. Exchange and correlation functionals were described within Perdew–Burke–Ernzerhof generalized gradient approximation (PBE-GGA)³⁷ with the GGA+U extension of the standard Dudarev implementation, where the on-site Coulomb interaction for localized orbitals in the transition metal is parametrized by $U_{\text{eff}} = U - J$. We apply the optimized effective interaction parameter U_{eff} for the transition metals ($U_{\text{eff}} = 4.0, 3.9, 5.7,$ and 6.1 eV for Mn, Fe, Co, and Ni, respectively) following Ong et al.³⁸ GGA+U calculations yield correct transition metal ion spin configurations (e.g., high spin configuration for Fe^{4+}O_6), though simply applying PBE-GGA results in low spin electronic configurations (e.g., low spin configuration for Fe^{4+}O_6). Minimum energy pathways and the activation energies were calculated by using the nudged elastic band method.³⁹

The supercell for O3-type NaTMO_2 consists of $4 \times 4 \times 1$ conventional unit cells (48 formula units). A $2 \times 2 \times 2$ k -point

Table 2. Pawley Fit of the Diffraction Data Corresponding to Cycled NaFeO₂ with 4.5 V High Cutoff Voltage, with a Space Group of *I*4₁/*amd*, *Fd* $\bar{3}$ *m*, *R* $\bar{3}$ *m*, *R* $\bar{3}$ *m* (O3), and *C*2/*m* (O'3)

	<i>a</i> (Å)	<i>b</i> (Å)	<i>c</i> (Å)	α (deg)	β (deg)	γ (deg)	<i>R</i> _{wp}
<i>Fd</i> $\bar{3}$ <i>m</i> (spinel)	8.4439(6)	8.4439(6)	8.4439(6)	90	90	90	8.37
<i>R</i> $\bar{3}$ <i>m</i> (hexagonal-distorted spinel)	5.971(1)	5.971(1)	14.739(5)	90	90	120	8.24
<i>I</i> 4 ₁ / <i>amd</i> (tetragonal-distorted spinel)	5.9291(8)	5.9291(8)	8.449(1)	90	90	90	8.13
<i>R</i> $\bar{3}$ <i>m</i> (O3)	2.9856(4)	2.9856(4)	14.679(3)	90	90	120	8.31
<i>C</i> 2/ <i>m</i> (O'3)	5.176(1)	2.929(1)	5.211(1)	90	109.31(1)	90	8.08

sampling were used in all simulations. To model compounds at high voltage with dilute Na concentrations, only one Na atom was kept in the supercell. The lattice parameters in the *ab* plane of fully sodiated phase were fully optimized by DFT and then fixed for NEB calculations. Na diffusion modeling was performed with various interlayer distances, corresponding to the experimental *c* lattice parameters obtained from *in situ* XRD.

3. RESULTS AND DISCUSSION

O3 and P3 are two typical stacking types of the oxygen atomic layers in layered NaTMO₂.⁴⁰ In all structures with O3 stacking,

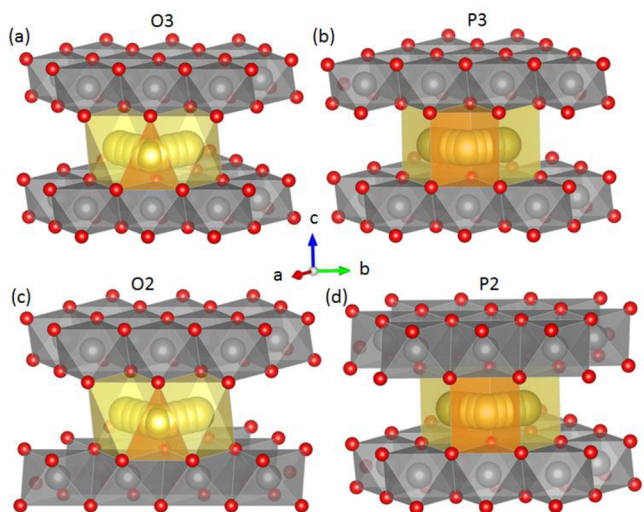


Figure 2. Na diffusion path in layered NaTMO₂ (TM = Fe, Co, Ni, ...) with four typical oxygen stackings of (a) O3, (b) P3, (c) O2, and (d) P2. Oxygen ions are colored in red; transition metal cations are in gray; sodium ions are in yellow. The stable sites (octahedral for O3 and O2; prismatic for P3 and P2) are colored as yellow, and the transition or activated sites (tetrahedral for O3 and O2; prismatic for P3 and P2) are colored in orange.

Na diffuses between neighboring octahedral sites through the activated tetrahedral site, while in P3 stacking Na diffuses between neighboring prismatic sites through the transient prismatic site, as shown in Figure 2a,b.^{30,41} All O3-type NaTMO₂ compounds show a clear O3–P3 transition at around 25% Na-ion extraction.^{6,14,20,21} A transition back to the O3 stacking at the later stage of charge has been observed in several *in situ* X-ray diffraction (XRD) measurements.^{6,20} In the quaternary transition metal layered compound MFCN, the new O3 phase that forms at high voltage shows a significant amount of reversible capacity of 25 mAh/g even though the interslab distance decreases dramatically at the end of charge.⁶ This extra capacity coming from the reversibility of the high-voltage O3 phase leads to high total capacities for several Fe-containing materials. The high initial discharge capacity and energy density of MFCN motivated us to study a series of transition metal

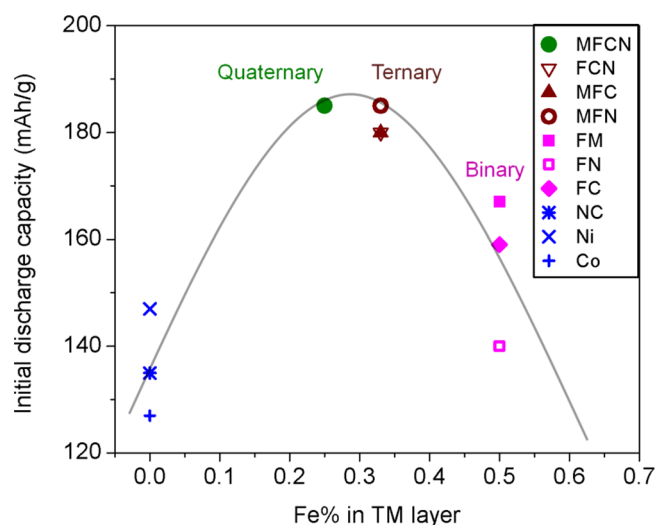


Figure 3. Initial discharge capacity of layered NaTMO₂ compounds with different transition metal combinations plotted as a function of Fe composition. Co (Ni) stands for NaCoO₂ (NaNiO₂). Compounds are listed by their TM content with M = Mn, F = Fe, C = Co, and N = Ni, and all compounds contain their TM in equal proportions (e.g., MFCN stands for Na(Mn_{1/4}Fe_{1/4}Co_{1/4}Ni_{1/4})O₂). More details can be found in Table 1. All cells were cycled at C/10 rate with 4.5 V high cutoff voltage.

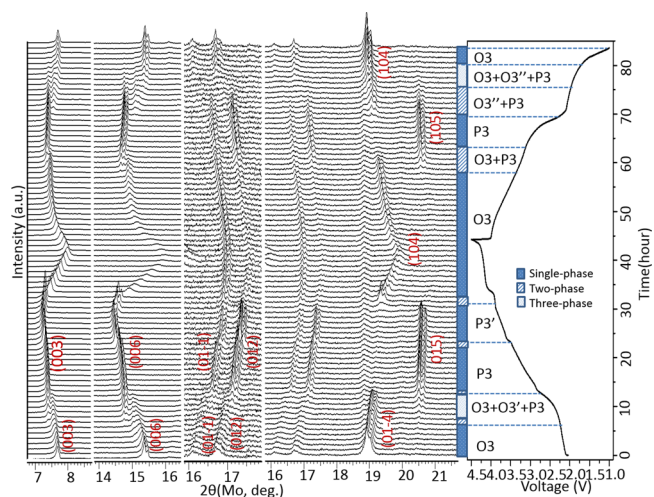


Figure 4. Structural evolution of MFC from *in situ* XRD in the first cycle at C/50 rate.

combinations picked from Mn, Fe, Co, and Ni, as listed in Table 1. By plotting the initial discharge capacity of various NaTMO₂ compounds from Table 1 versus their Fe composition (Figure 3), one can observe that the maximum capacity is obtained when ~30% Fe composition is present in the TM layer. The simple dome-shaped relationship in Figure 3

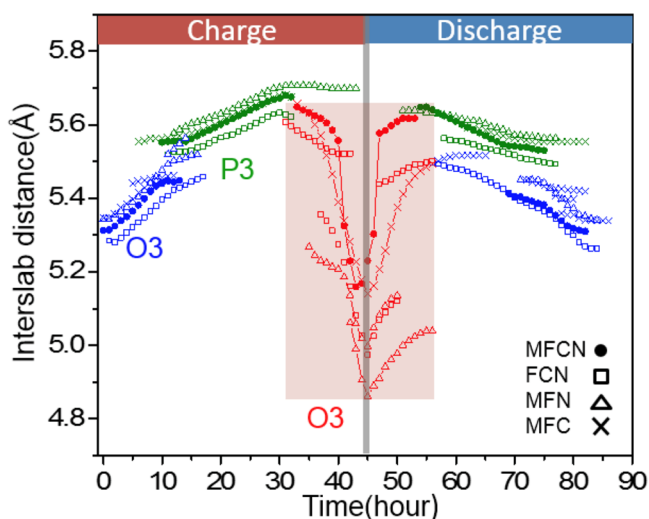


Figure 5. Interplanar distance of layered NaTMO₂ compounds with different ternary and quaternary transition metal combinations upon charge and discharge measured by *in situ* XRD. O3 phases at the beginning of charge and end of discharge are marked in blue. P3 phases in the middle range of charge and discharge are marked by green. O3 phases at the end of charge and early stage of discharge are marked by red. The labels of compounds follow the same rule as Figure 3 and Table 1. All *in situ* XRD batteries were cycled at C/50 rate with 4.5 V high cutoff voltage.

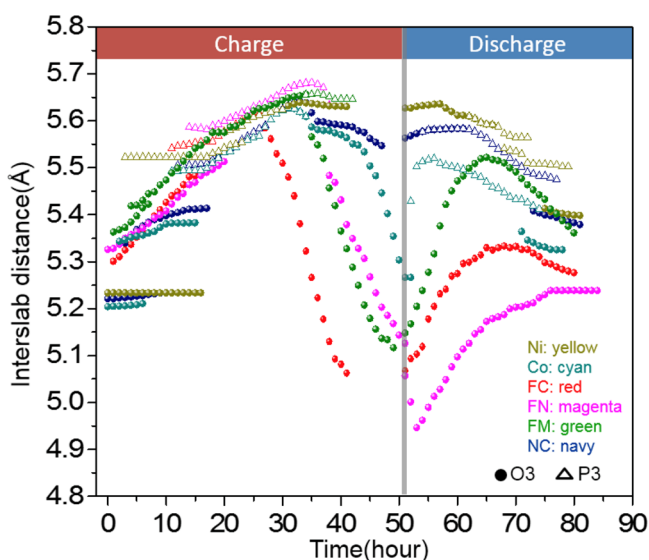


Figure 6. Interplanar distance of layered NaTMO₂ compounds with different binary and single transition metal combinations upon charge and discharge measured by *in situ* XRD. O3 phases are represented by dots, and P3 are represented by empty triangles. Compounds are differentiated by colors with their labels in the legend following the same rule as Figure 3 and Table 1. All *in situ* cells were cycled between 2 and 4.5 V at C/50 rate.

indicates that two competing mechanisms related to Fe may be playing a role: one assists the compound to reach higher capacity and the other to decrease the capacity. We use a combination of experimental and theoretical approaches to investigate this underlying physics.

Using *in situ* XRD, we observed P3–O3 transitions at the later stage of charge for all the compounds listed in Table 1. For example, the *in situ* XRD result of MFC (Figure 4) shows a

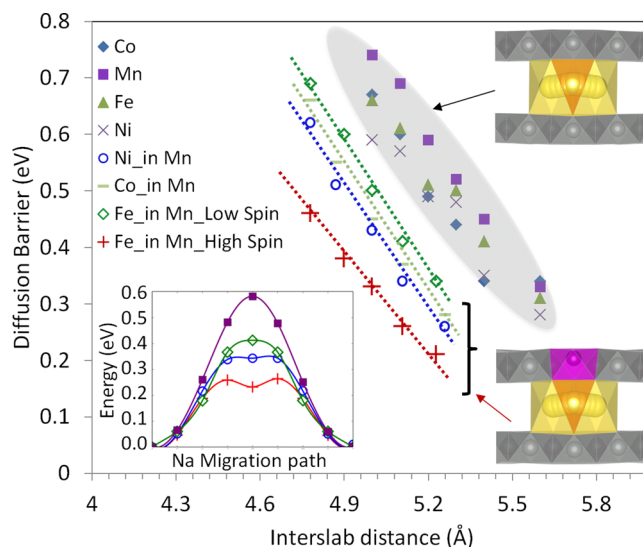


Figure 7. DFT calculated Na activation energies in layered NaTMO₂ with different transition metal combinations at various interslab distances. The labels of Mn, Fe, Co, and Ni in the legend stand for the transition metal cations TM in the NaTMO₂. Ni_{in} Mn stands for an isolated Ni (adjacent to the Na migration path) embedded in the Mn surroundings, etc. For Fe_{in} Mn, both high spin and low spin electronic configurations of Fe are calculated. The upper right inset shows the calculated Na diffusiton path for NaTMO₂ with a single type of transition metal (gray). The lower right inset shows the Na diffusion path when Fe (purple octahedra) embedded in Mn surroundings (gray) is face-sharing with the activated state. Obvious buckling of Fe can be observed. The lower left inset shows the calculated profiles for Na migration at the interslab distance of 5.1 Å.

highly reversible structure evolution upon charge and discharge, including a clear P3–O3 transition together with a broad sodium composition range for the high-voltage O3 phase, distinguished by XRD refinement. The evolution of the interslab distances with level of desodiation for all the ternary and quaternary systems is summarized in Figure 5. The interslab distance can shrink from 5.7 Å at the beginning of the high-voltage O3 phase to as low as 4.8 Å at the end of charge. This process is largely reversible, and the interslab distance expands back upon discharge, indicating good Na diffusivity even at very low Na slab thicknesses. The reversible capacity of the high-voltage O3 phase and good reversibility upon discharge result in the high initial discharge capacities in these compounds. The structure evolution in the single and binary transition metal systems is different from the ternary and quaternary systems, as shown in Figure 6. The composition ranges of the high voltage O3 phases formed in the initial charge are significantly shrunk upon discharge, associated with unsymmetrical charge–discharge structural evolutions. This leads to reduced initial discharge capacities for single and binary transition metal systems. The asymmetry in structural evolution between charge and discharge indicates structural irreversibility associated with the emergence of high voltage O3 phases, and the Na diffusion can be very sluggish.

We now show that it is exactly the difference in Na mobility at the end of charge that distinguishes the compounds that perform well from those that do not. The Na migration energy as calculated with Density Functional Theory (DFT) in the O3 structures at different interslab distances (see Methods) is shown in Figure 7. The high Na diffusion barrier (beyond 600 meV) associated with small interslab distance below 5 Å

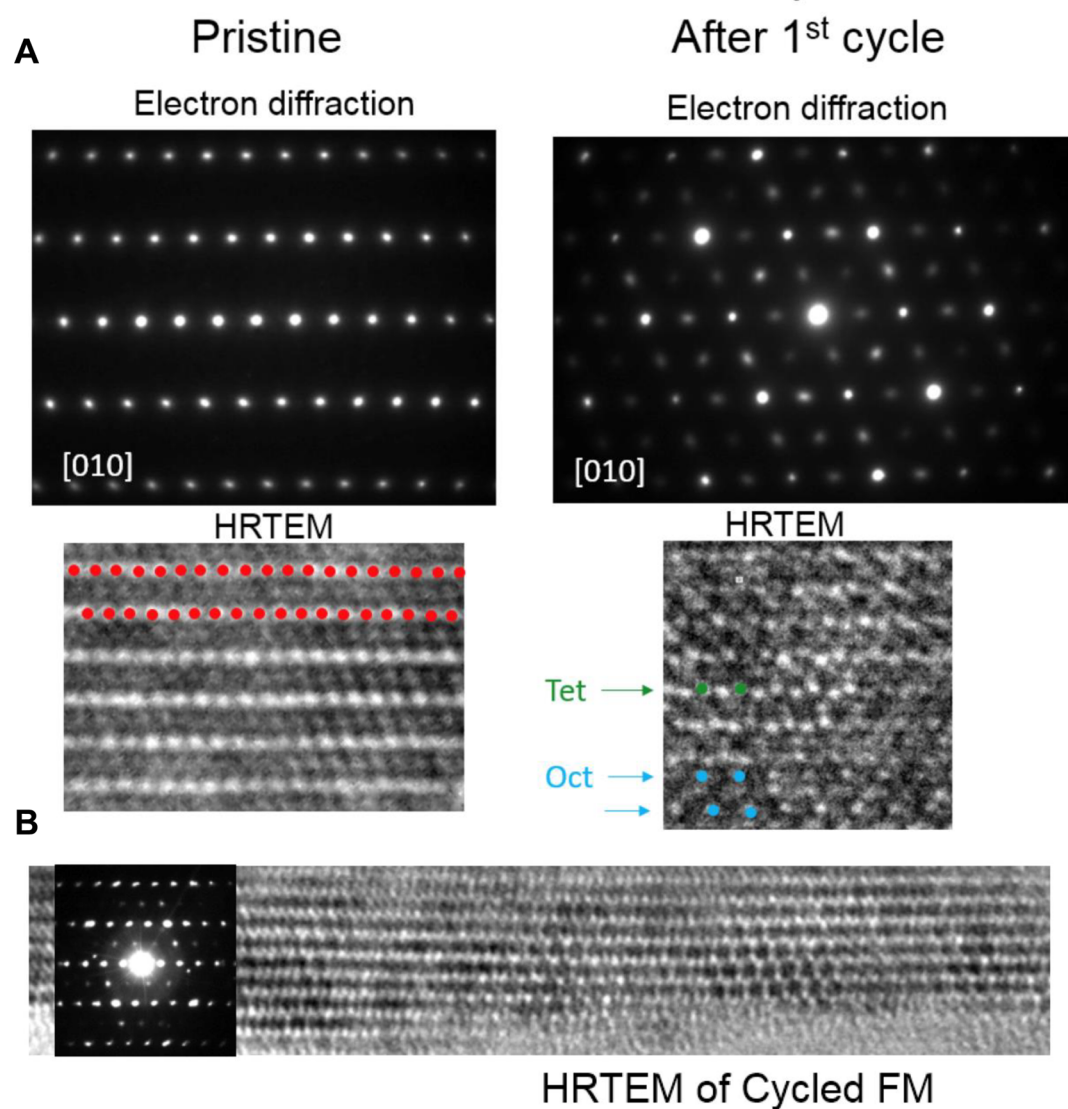


Figure 8. (A) Electron diffraction and HRTEM of NaFeO_2 after 1 cycle between 2 and 4.5 V at C/10 rate. Red dots label the transition metal columns; green dots label the migrated Fe to the tetrahedral sites; blue dots are migrated to the octahedral sites. (B) Electron diffraction and HRTEM of $\text{Na}(\text{Fe}_{1/2}\text{Mn}_{1/2})\text{O}_2$ after 1 cycle between 2 and 4.5 V at C/10 rate.

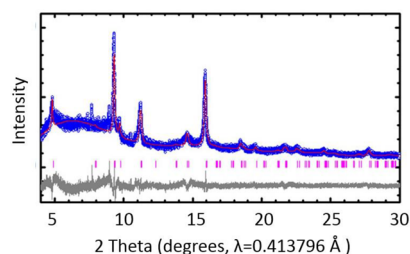


Figure 9. Pawley fit of the diffraction data corresponding to cycled NaFeO_2 with 4.5 V high cutoff voltage, with a space group of $I4_1/amd$ (tetragonal-distorted spinel) and lattice parameters of $a = b = 5.9291 \text{ \AA}$ and $c = 8.449 \text{ \AA}$. The observed, calculated, and difference patterns are shown in blue, red, and dark gray, respectively. Tick marks for the tetragonal lattice are shown in magenta. The results for all the possible space groups are shown in Table 2.

suggests poor Na diffusivity in many of the layered NaTMO_2 compounds. Only for the metal oxides that embed Fe in high spin configuration, such as $\text{Fe}_{\text{HS_in_MnO}_2}$ in Figure 7, is the

Na migration energy considerably lower. In such system, Na^+ passes through the tetrahedral site (Na_{tet}) face sharing with the high-spin Fe^{4+}O_6 embedded in an MnO_2 host. In contrast to the other systems, when Fe^{4+}O_6 is near the activated state, the calculation shows a significant buckling of the Fe–O bonds along the direction from Na_{tet} to Fe, as illustrated in the Figure 7 insets. The buckling increases the distance of Fe to the Na-ion as it passes through the face-sharing tetrahedral site. This effect significantly lowers the Na diffusion barrier, improving Na mobility at the top of charge. This mechanism is consistent with the calculated energy profile of Na along the migration path (Figure 7 inset) that dips considerably lower at the tetrahedral site when Fe is embedded in other transition metal surroundings, compared with other non-Fe systems. The shape of the migration energy at the tetrahedral site indicates a local energy minimum caused by the dynamic buckling of Fe.

It is worth noting that such Fe assisted Na migration only occurs when Fe^{4+}O_6 is in the JT-active high spin electronic configuration (Figure 1). If we force Fe to be in the low spin configuration in the DFT calculation (see Methods), the

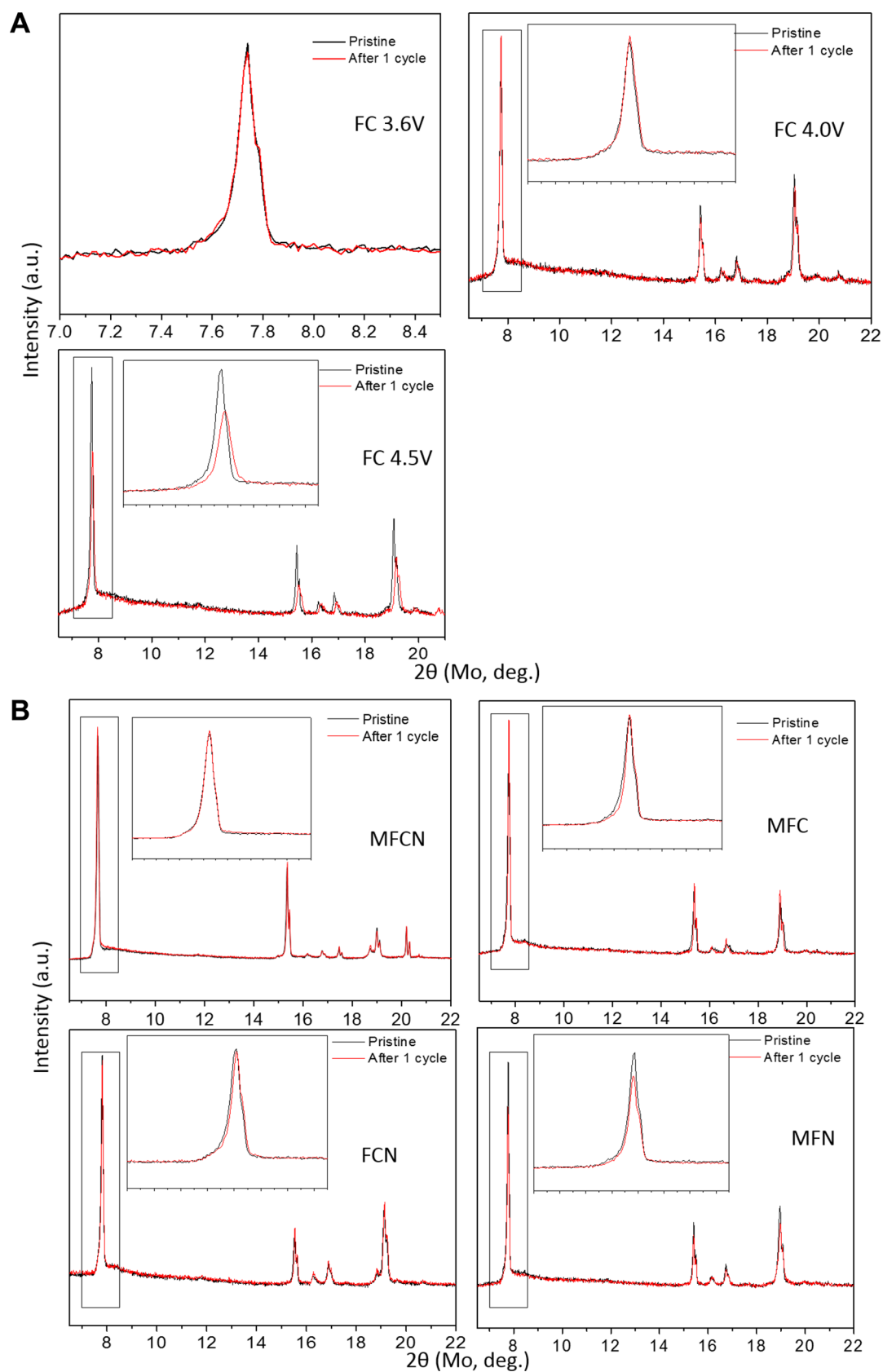


Figure 10. (A) Comparison of *in situ* XRD patterns obtained for pristine FC and after one cycle at several different cutoff voltages at C/50 rate. The insets highlight the marked 003 peak region. (B) Comparison of XRD patterns of pristine layered compound and the one after 1 cycle from *in situ* XRD measurement for MFC, FCN, MFN, and MFCN. The insets show the marked 003 peak region. All *in situ* batteries were cycled at C/10 rate with 4.5 V high cutoff voltage.

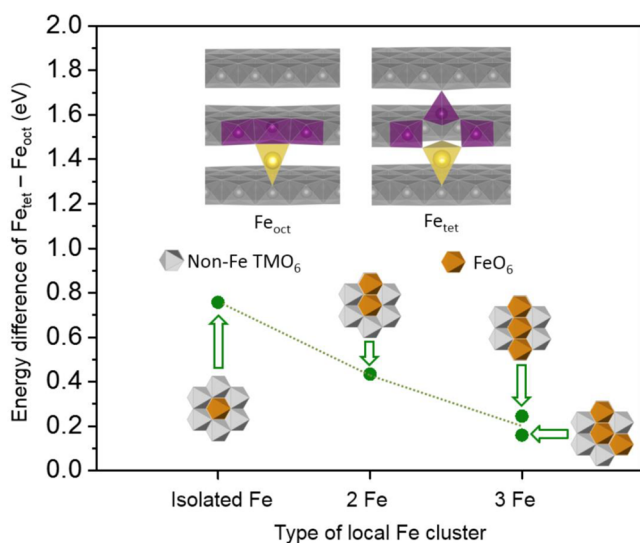


Figure 11. Calculated energy penalty for Fe migration from an octahedral site in the TM layer to a tetrahedral site in the Na layer of $NaTMO_2$. Results are shown with different types of local Fe clusters, as illustrated in the insets pointed to the data. The upper insets show the models for Fe_{tet} with Fe sitting in the tetrahedral site of the Na layer (after migration) and Fe_{oct} with Fe sitting in the original octahedral site of the transition metal layer (before migration). Na ion is always in the tetrahedral site as shown in the inset in all the calculations.

migration barrier becomes as high as those in non-Fe containing systems as illustrated in Figure 7 (Fe in Mn_Low Spin). This computational experiment clearly demonstrates that it is the JT activity of high spin $Fe^{4+}O_6$ that provides the buckling capability to lower the Na migration barrier. The JT distortion of the $Fe^{4+}O_6$ octahedron in layered $NaTMO_2$ is of the Q3-mode type^{42,43} with two long Fe–O bonds and four short Fe–O bonds, lowering the local octahedron symmetry from O_h to D_{2h} . This JT distortion assisted Na diffusion explains the capacity increase with increasing Fe composition up to around 30% shown in Figure 3. The capacity drop beyond 30% Fe composition is caused by the JT distortion assisted Fe migration to the Na layer, as we will discuss below.

$NaFeO_2$ becomes electrochemically inactive when charged beyond 3.3 V corresponding to 30% Na extraction,¹⁷ as shown in Table 1. Fe migration into the Na layer in $NaFeO_2$ can be directly observed by high resolution transmission electron microscopy (HRTEM) as shown in Figure 8A. The electron diffraction pattern suggests the formation of a spinel-like structure after Fe migration, consistent with our HRTEM result showing some ordered occupancy of Fe in both the tetrahedral and octahedral sites of the Na layer. The spinel-like structure suggested by TEM is also consistent with our synchrotron XRD refinement in Figure 9. These migrated Fe ions will largely impede the Na diffusion and make the compound electrochemically inactive.

For the binary transition metal systems with 50% Fe, including FM, FC, and FN, the structure is not completely reversible after the first electrochemical cycle once the initial charge goes beyond a certain level of Na extraction. In these binary transition metal compounds, TEM still shows a certain degree of local transition metal migration but less serious than in $NaFeO_2$, as illustrated in Figure 8B using FM as an example. As shown in Figure 10A using FC as an example, the interslab distance after the first discharge shrinks below the value of the

pristine structure when charged above 4 V, suggesting the migration of transition metal into the sodium layer. This is consistent with our DFT simulation indicating that, if transition metal ions are located in the tetrahedral sites of the Na layer with sodium vacancies around the migrated TM ion in the sodiated structure, the interslab distance shrinks below the pristine value.

In the ternary and quaternary transition metal systems, the structure evolution is largely reversible, as shown in Figure 4 for MFC and reported in previous literature for MFCN.⁶ After the first cycle, the structure transforms back to the pristine structure even these compounds were charged to 4.5 V, as shown in Figure 10B. No obvious transition metal migration in these ternary and quaternary transition metal systems is observed by HRTEM. We also confirmed with HRTEM the absence of migrated transition metal ions after an electrochemical cycle in the Fe-free systems such as in $NaNiO_2$, $NaCoO_2$, and NC. All the above experimental results combined suggest that Fe migrates less with decreasing Fe composition and that below around 30% Fe composition the Fe migration is fully suppressed.

We further validate the idea of composition-dependent Fe migration with DFT calculations. Figure 11 shows that an isolated Fe has a relatively high energy penalty above 700 meV to prevent its migration. On the other hand, the calculated energy penalty for Fe migration from the TM layer into the Na layer drops significantly when Fe starts to form local clusters. The inset in Figure 11 clearly shows that, when Fe clusters together, the distortion of a neighboring JT active Fe ion in the TM layer can accommodate the shortening of the Fe–O bonds in the tetrahedron associated with a migrating Fe. This cooperative local distortion significantly lowers the energy of tetrahedral Fe in the Na layer and thus greatly enhances the probability of the Fe migration. We notice that in the triangular lattice statistically the Fe ions start to form local clusters with edge-sharing FeO_6 octahedra beyond around 33% Fe composition. This Jahn–Teller related Fe migration explains the optimal Fe composition to be around 33% in Figure 3, beyond which the increasing probability of local Fe migration gradually deteriorates the electrochemical activity of the compound.

We expect the mechanisms of JT distortion assisted Na diffusion and Fe migration found in O3- $NaTMO_2$ to be transferable to other sodium structures. In P2 layered compounds (Figure 2d), the possible evolution of P2 (Figure 2d) to O2 (Figure 2c) or OP4 structures at a later stage of charge^{7,25,44} could potentially lead to similar issues of Fe migration into the Na layer. Our simulation demonstrates that the JT distortion assisted Fe migration into the tetrahedral site in the O2 structure leads to a lower energy penalty when Fe cluster forms. Furthermore, for many other structures like beta- $NaMnO_2$ or channel structures,^{31,32} the JT distortion assisted Na diffusion mechanism will be active as long as the Na diffusion path involves an active site face-shared with a JT active transition metal octahedron (e.g., $Fe^{4+}O_6$).

4. CONCLUSION

In conclusion, we uncovered a remarkable synergy between an esoteric piece of physics and practical aspects of Na mobility to create high capacity Na-cathode materials. The JT activity of $Fe^{4+}O_6$ creates two competitive mechanisms which when carefully balanced can create compounds with high Na-storage capacity. On one hand, its ability, through the electronic

degeneracy of the d_{HS}^4 state, to buckle and distort Fe–O bonds facilitates the Na diffusion when the space along the diffusion pathway is limited, a critically limiting factor in the layered structure at the end of charge. The structural flexibility provided by the JT active transition metal oxygen octahedra effectively assists the Na to squeeze through the bottleneck in the diffusion pathway. On the other hand, the soft-mode behavior of Fe^{4+}O_6 can also assist Fe migration into the Na layer when too much Fe is present, an effect which is detrimental to the capacity. Our understanding here provides new guidelines to design high capacity and energy density Na intercalation cathode and anode compounds. It is truly exciting that JT-deformation finding its origin in symmetry rules that describe orbital energy degeneracy may find practical application in large-scale electricity storage devices.

AUTHOR INFORMATION

Corresponding Author

*E-mail: gceder@berkeley.edu.

Notes

The authors declare no competing financial interest.

ACKNOWLEDGMENTS

This work was supported by the Samsung Advanced Institute of Technology. Computational resources from the National Energy Research Scientific Computing Center (NERSC) and from the Extreme Science and Engineering Discovery Environment (XSEDE) are gratefully acknowledged. Use of the Advanced Photon Source at Argonne National Laboratory was supported by the U.S. Department of Energy, Office of Science, Office of Basic Energy Sciences, under Contract No. DE-AC02-06CH11357.

REFERENCES

- (1) Kim, S.-W.; Seo, D.-H.; Ma, X.; Ceder, G.; Kang, K. Electrode Materials for Rechargeable Sodium-Ion Batteries: Potential Alternatives to Current Lithium-Ion Batteries. *Adv. Energy Mater.* **2012**, *2*, 710–721.
- (2) Yabuuchi, N.; Kubota, K.; Dahbi, M.; Komaba, S. Research Development on Sodium-Ion Batteries. *Chem. Rev.* **2014**, *114*, 11636–11682.
- (3) Pan, H.; Hu, Y.-S.; Chen, L. Room-Temperature Stationary Sodium-Ion Batteries for Large-Scale Electric Energy Storage. *Energy Environ. Sci.* **2013**, *6*, 2338–2360.
- (4) Han, M. H.; Gonzalo, E.; Singh, G.; Rojo, T. A Comprehensive Review of Sodium Layered Oxide: Powerful Cathode for Na-ion Battery. *Energy Environ. Sci.* **2015**, *8*, 81–102.
- (5) Hasa, I.; Buchholz, D.; Passerini, S.; Scrosati, B.; Hassoun, J. High Performance $\text{Na}_{0.5}\text{Ni}_{0.23}\text{Fe}_{0.13}\text{Mn}_{0.63}\text{O}_2$ Cathode for Sodium-Ion Batteries. *Adv. Energy Mater.* **2014**, *4*, 1400083.
- (6) Li, X.; Wu, D.; Zhou, Y.-N.; Liu, L.; Yang, X.-Q.; Ceder, G. O₃-type $\text{Na}(\text{Mn}_{0.25}\text{Fe}_{0.25}\text{Co}_{0.25}\text{Ni}_{0.25})\text{O}_2$: A Quaternary Layered Cathode Compound for Rechargeable Na Ion Batteries. *Electrochem. Commun.* **2014**, *49*, 51–54.
- (7) Yabuuchi, N.; Kajiyama, M.; Iwatate, J.; Nishikawa, H.; Hitomi, S.; Okuyama, R.; Usui, R.; Yamada, Y.; Komaba, S. P₂-type $\text{Na}_x[\text{Fe}_{1/2}\text{Mn}_{1/2}]\text{O}_2$ Made from Earth-Abundant Elements for Rechargeable Na Batteries. *Nat. Mater.* **2012**, *11*, 512–517.
- (8) Brese, N. E.; O’Keeffe, M.; Von Dreele, R. B.; Young, V. G., Jr. Crystal Structures of NaCuO_2 and KCuO_2 by Neutron Diffraction. *J. Solid State Chem.* **1989**, *83*, 1–7.
- (9) Delmas, C.; Saadoun, I.; Dordor, P. Molecular Crystals and Liquid Effect of Cobalt Substitution on the Jahn-Teller Distortion of the NaNiO_2 Layered Oxide. *Mol. Cryst. Liq. Cryst. Sci. Technol., Sect. A* **1994**, *244*, 337–342.
- (10) Komaba, S.; Takeji, C.; Nakayama, T.; Ogata, A.; Yabuuchi, N. Electrochemical Intercalation Activity of Layered NaCrO_2 vs. LiCrO_2 . *Electrochem. Commun.* **2010**, *12*, 355–358.
- (11) Berthelot, R.; Carlier, D.; Delmas, C. Electrochemical Investigation of the $\text{P2-Na}_x\text{CoO}_2$ Phase Diagram. *Nat. Mater.* **2011**, *10*, 74–80.
- (12) Ma, X.; Chen, H.; Ceder, G. Electrochemical Properties of Monoclinic NaMnO_2 . *J. Electrochem. Soc.* **2011**, *158*, A1307.
- (13) Kim, D.; Lee, E.; Slater, M.; Lu, W.; Rood, S.; Johnson, C. S. Layered $\text{Na}[\text{Ni}_{1/3}\text{Fe}_{1/3}\text{Mn}_{1/3}]\text{O}_2$ Cathodes for Na-Ion Battery Application. *Electrochem. Commun.* **2012**, *18*, 66–69.
- (14) Sathiyaa, M.; Hemalatha, K.; Ramesha, K.; Tarascon, J.-M.; Prakash, A. S. Synthesis, Structure, and Electrochemical Properties of the Layered Sodium Insertion Cathode Material: $\text{NaNi}_{1/3}\text{Mn}_{1/3}\text{Co}_{1/3}\text{O}_2$. *Chem. Mater.* **2012**, *24*, 1846–1853.
- (15) Vassilaras, P.; Ma, X.; Li, X.; Ceder, G. Electrochemical Properties of Monoclinic NaNiO_2 . *J. Electrochem. Soc.* **2013**, *160*, A207–A211.
- (16) Xia, X.; Dahn, J. R. NaCrO_2 is a Fundamentally Safe Positive Electrode Material for Sodium-Ion Batteries with Liquid Electrolytes. *Electrochem. Solid-State Lett.* **2012**, *15*, A1–A4.
- (17) Yabuuchi, N.; Yoshida, H.; Komaba, S. Crystal Structures and Electrode Performance of $\alpha\text{-NaFeO}_2$ for Rechargeable Sodium Batteries. *Electrochemistry* **2012**, *80*, 716–719.
- (18) Guignard, M.; Didier, C.; Darriet, J.; Bordet, P.; Elkaim, E.; Delmas, C. $\text{P2-Na}_x\text{VO}_2$ System as Electrodes for Batteries and Electron-Related Materials. *Nat. Mater.* **2013**, *12*, 74–80.
- (19) Yoshida, H.; Yabuuchi, N.; Komaba, S. $\text{NaFe}_{0.5}\text{Co}_{0.5}\text{O}_2$ as High Energy and Power Positive Electrode for Na-Ion Batteries. *Electrochem. Commun.* **2013**, *34*, 60–63.
- (20) Han, M. H.; Gonzalo, E.; Casas-Cabanas, M.; Rojo, T. Structural Evolution and Electrochemistry of Monoclinic NaNiO_2 upon the First Cycling Process. *J. Power Sources* **2014**, *258*, 266–271.
- (21) Lei, Y.; Li, X.; Liu, L.; Ceder, G. Synthesis and Stoichiometry of Different Layered Sodium Cobalt Oxides. *Chem. Mater.* **2014**, *26*, 5288–5296.
- (22) Vassilaras, P.; Toumar, A. J.; Ceder, G. Electrochemical Properties of $\text{NaNi}_{1/3}\text{Co}_{1/3}\text{Fe}_{1/3}\text{O}_2$ as A Cathode Material for Na-Ion Batteries. *Electrochem. Commun.* **2014**, *38*, 79–81.
- (23) Wang, X.; Liu, G.; Iwao, T.; Okubo, M.; Yamada, A. Role of Ligand-To-Metal Charge Transfer in O₃-type NaFeO_2 – NaNiO_2 Solid Solution For Enhanced Electrochemical Properties. *J. Phys. Chem. C* **2014**, *118*, 2970–2976.
- (24) Xu, S.-Y.; Wu, X.-Y.; Li, Y.-M.; Hu, Y.-S.; Chen, L.-Q. Novel Copper Redox-Based Cathode Materials For Room-Temperature Sodium-Ion Batteries. *Chin. Phys. B* **2014**, *23*, 118202.
- (25) Talaie, E.; Duffort, V.; Smith, H.; Fultz, B.; Nazar, L. Structure of the High Voltage Phase of Layered $\text{P2-Na}_{2/3-x}[\text{Mn}_{1/2}\text{Fe}_{1/2}]\text{O}_2$ and the Positive Effect of Ni Substitution on its Stability. *Energy Environ. Sci.* **2015**, *8*, 2512–2523.
- (26) Wu, D.; Li, X.; Xu, B.; Twu, N.; Liu, L.; Ceder, G. NaTiO_2 : A Layered Anode Material for Sodium-Ion Batteries. *Energy Environ. Sci.* **2015**, *8*, 195–202.
- (27) Komaba, S.; Yabuuchi, N.; Nakayama, T.; Ogata, A.; Ishikawa, T.; Nakai, I. Study on the Reversible Electrode Reaction of $\text{Na}_{1-x}\text{Ni}_{0.5}\text{Mn}_{0.5}\text{O}_2$ for a Rechargeable Sodium-ion Battery. *Inorg. Chem.* **2012**, *51*, 6211–6220.
- (28) Kim, S.; Ma, X.; Ong, S. P.; Ceder, G. A Comparison of Destabilization Mechanisms of The Layered Na_xMO_2 and Li_xMO_2 Compounds upon Alkali De-Intercalation. *Phys. Chem. Chem. Phys.* **2012**, *14*, 15571.
- (29) Van der Ven, A.; Ceder, G. Lithium Diffusion Mechanisms in Layered Intercalation Compounds. *J. Power Sources* **2001**, *97*–98, 529–531.
- (30) Van Der Ven, A.; Ceder, G. Lithium Diffusion in Layered Li_xCoO_2 . *Electrochem. Solid-State Lett.* **2000**, *3*, 301–304.
- (31) Wang, Y.; Liu, J.; Lee, B.; Qiao, R.; Yang, Z.; Xu, S.; Yu, X.; Gu, L.; Hu, Y.-S.; Yang, W.; Kang, K.; Li, H.; Yang, X.-Q.; Chen, L.; Huang, X. Ti-substituted Tunnel-type $\text{Na}_{0.44}\text{MnO}_2$ Oxide as A

Negative Electrode for Aqueous Sodium-Ion Batteries. *Nat. Commun.* **2015**, *6*, 6401.

(32) Billaud, J.; Clement, J.; Armstrong, A. R.; Rozier, P.; Grey, C. P.; Bruce, P. G. β -NaMnO₂: A High-Performance Cathode for Sodium-Ion Batteries. *J. Am. Chem. Soc.* **2014**, *136*, 17243–17248.

(33) Li, X.; Ma, X.; Su, D.; Liu, L.; Chisnell, R.; Ong, S. P.; Chen, H.; Toumar, A.; Idrobo, J.; Lei, Y.; Bai, J.; Wang, F.; Lynn, J. W.; Lee, Y. S.; Ceder, G. Direct Visualization of The Jahn–Teller Effect Coupled to Na Ordering in Na_{5/8}MnO₂. *Nat. Mater.* **2014**, *13*, 586–592.

(34) Marianetti, C.; Morgan, D.; Ceder, G. First-Principles Investigation of The Cooperative Jahn-Teller Effect for Octahedrally Coordinated Transition-Metal Ions. *Phys. Rev. B: Condens. Matter Mater. Phys.* **2001**, *63*, 1–15.

(35) Bussmann-Holder, A.; Muller, K. A. *100 Years of Superconductivity*; CRC Press: Boca Raton, FL, 2011; pp 236–244.

(36) Kresse, G.; Furthmüller, J. Efficient Iterative Schemes for Ab Initio Total-Energy Calculations Using A Plane-Wave Basis Set. *Phys. Rev. B: Condens. Matter Mater. Phys.* **1996**, *54*, 11169–11186.

(37) Perdew, J. P.; Burke, K.; Ernzerhof, M. Generalized Gradient Approximation Made Simple. *Phys. Rev. Lett.* **1996**, *77*, 3865–3868.

(38) Ong, S. P.; Chevrier, V. L.; Hautier, G.; Jain, A.; Moore, C.; Kim, S.; Ma, X.; Ceder, G. Voltage, Stability and Diffusion Barrier Differences Between Sodium-Ion and Lithium-Ion Intercalation Materials. *Energy Environ. Sci.* **2011**, *4*, 3680–3688.

(39) Henkelman, G.; Uberuaga, B. P.; Jónsson, H. A Climbing Image Nudged Elastic Band Method for Finding Saddle Points and Minimum Energy Paths. *J. Chem. Phys.* **2000**, *113*, 9901.

(40) Delmas, C.; Fouassier, C.; Hagenmuller, P. Structural Classification and Properties of the Layered Oxides. *Physica B+C* **1980**, *99*, 81–85.

(41) Kang, K.; Meng, Y. S.; Breger, J.; Grey, C. P.; Ceder, G. Electrodes with High Power and High Capacity for Rechargeable Lithium Batteries. *Science* **2006**, *311*, 977–980.

(42) Bersuker, B. I. *The Jahn-Teller Effect*; Cambridge University Press: Cambridge, UK, 2006.

(43) Goodenough, J. B. Jahn-Teller Phenomena in Solids. *Annu. Rev. Mater. Sci.* **1998**, *28*, 1–27.

(44) Clément, R. J.; Bruce, P. G.; Grey, C. P. Review: Manganese-Based P2-Type Transition Metal Oxides as Sodium-Ion Battery Cathode Materials. *J. Electrochem. Soc.* **2015**, *162*, A2589–A2604.